Photonic crystal bandedge membrane lasers on silicon

SHIH-CHIA LIU,[1] DEYIN ZHAO,[1] YONGHAO LIU,[1] HONGJUN YANG,[1] YUZE SUN,[1] ZHENGQIANG MA,[2] CARL REUTERSKIÖLD-HEDLUND,[3] MATTIAS HAMMAR,[3] AND WEIDONG ZHOU[1,*]

[1]*Department of Electrical Engineering, University of Texas at Arlington, Texas 76019, USA*
[2]*Department of Electrical and Computer Engineering, University of Wisconsin-Madison, Madison, Wisconsin 53706, USA*
[3]*KTH-Royal Institute of Technology, School of Information and Communication Technology, Electrum 229, 164 40 Kista, Sweden*
Corresponding author: wzhou@uta.edu

We report here the design and experimental demonstration of optically pumped photonic crystal bandedge membrane lasers on silicon-on-insulator (SOI) and on bulk silicon (Si) substrates, based on heterogeneously integrated InGaAsP multi-quantum-well membrane layers transfer printed onto patterned photonic crystal cavities. Single-mode lasing under room-temperature operation was observed at 1542 nm, with excellent side mode suppression ratio greater than 31.5 dB, for the laser built on SOI substrate. For the laser built on bulk Si substrate, single-mode lasing was also achieved at 1452 nm with much lower thermal resistance, as compared to that of the laser built on SOI substrates. Such improved thermal characteristics are favorable for lasers operating potentially at higher temperatures and higher power. © 2017 Optical Society of America

1. INTRODUCTION

Remarkable progress has been made over recent years on silicon (Si) photonics by utilizing the complementary metal-oxide-semiconductor (CMOS)-compatible process, which is capable of producing devices and integrated circuits (IC) chips at low cost and in mass volumes [1–3]. CMOS-compatible lasers on Si remain an active and challenging area of research for integrated Si photonics [4–8]. The heterogeneous integration of III-V semiconductor with Si cavity seems to be one of the most promising approaches. Various III-V/Si hybrid lasers have been reported, by either bonding III-V gain materials to Si [9,10] or by growing III-V materials directly on Si [11–13]. By utilizing the transfer printing technique, we reported earlier membrane-reflector vertical-cavity surface-emitting lasers on Si [14]. We also reported earlier low temperature photonic crystal surface-emitting lasers (PCSELs) on silicon-on-insulator (SOI) substrates, based on the photonic crystal (PC) band edge effect [15]. Here we experimentally demonstrate a room-temperature PC bandedge membrane laser on SOI substrates by optimizing the cavity design and improving the fabrication quality. The experiment results are also correlated to theoretical and numerical analysis in order to clarify the design key factors that are essential for room-temperature operation.

Despite the experimental advances that have recently been integrated with the Si substrate, most III-V/Si hybrid lasers reported so far were demonstrated on SOI substrates. The use of SOI substrates still presents a substrate incompatibility issue with conventional Si electronic chips, largely built directly on bulk Si substrates. Additionally, the presence of a low-index buried oxide (BOX) layer underneath the functional Si layer also limits the thermal performance of the photonic devices built on it, especially, lasers, due to the relatively low thermal conductivity of oxide. Thus, it is of great importance to explore Si photonics built directly on bulk Si substrates [16,17]. Recently, photonic functions and device integration architectures have been being reported along this direction, including both multilayer 3D photonic integration and vertical-cavity surface-emitting laser (VCSEL)-based surface-emitting schemes [18,19]. This allows efficient heat removal from the active gain medium. Moreover, thermal simulations showed that lasers integrated with bulk Si substrates demonstrate low thermal resistance, which facilitates high lasing efficiency and high temperature operation [20,21].

In this paper, we report the demonstration of the PC bandedge membrane laser on SOI substrate directly built on bulk Si substrate based on the transfer printing technique.

Single-mode lasing under room-temperature operation from PC bandedge membrane laser on SOI substrate was observed with narrow linewidth and excellent side mode suppression ratio (SMSR). In addition, thermal performance was also investigated to realize efficient heat dissipation and low thermal resistance afforded by the architecture of PC bandedge membrane laser on bulk Si substrate.

2. CAVITY DESIGN

A schematic of the PC bandedge membrane laser on Si is shown in Fig. 1(a). The laser cavity consists of an InGaAsP multi-quantum-well (MQW) membrane heterostructure, and a Si-PC slab on SOI substrate with BOX layer thickness of 400 nm. The InGaAsP MQW layer design is based on the previously reported low temperature PC bandedge membrane laser, which consists of a bottom InGaAs contact layer, top and bottom InP cladding layers, and eight pairs of strain-compensated $In_{0.76}Ga_{0.24}As_{0.83}P_{0.17}/In_{0.485}Ga_{0.515}As_{0.83}P_{0.17}$ with the center emission wavelength of 1535 nm at room temperature [15]. In order to achieve room-temperature operation in PC bandedge membrane lasers in such a cavity, it is highly desirable to design a cavity with the following characteristics: (1) Two dimension (2D) square lattices Si-PC structure is designed to have a lattice constant of 480 nm, based on the second-order Bragg diffraction condition [22–28]; (2) the cavity mode distribution should match with MQW emission peak, with the hole radius and thickness of Si-PC slab designed to be 72 nm ($r = 0.15a$) and 190 nm, respectively; (3) the separation distance between the InGaAsP MQW layer and Si-PC slab is reduced to enhance the in-plane coupling efficiency [29,30].

A. Mode Distribution

The approximate refractive index n_{eff} of the whole cavity (InGaAsP MQW active layer and Si-PC) is around 3.2 based on the average dielectric constant in the initial design. In order to achieve surface-emitting output for the emission wavelength close to the communication wavelength range of 1550 nm, the

lattice constant a of the cavity is calculated to be 480 nm according to second Bragg diffraction condition $a = \lambda/n_{eff}$. Second, the air hole radius is designed to be 72 nm ($r = 0.15a$) in order to reduce the vertical radiation loss to obtain high Q and low threshold [15,23]. Finally, to optimize the cavity mode match with the MQW emission peak, the thickness of the Si-PC slab is chosen to be around 190 nm [31].

B. Band Diagram

The band diagram for the Si-PC bandedge lasing cavity is shown in Fig. 1(b). It is obtained from the Fano/guided resonances peaks or dips in the simulated reflection or transmission spectra according to the relation between the in-plane wave vector $k_\parallel$ and the incident angle θ, $k_\parallel = 2\pi/\lambda \cdot \sin\theta$ [32], where λ is the wavelength and θ is the incident angle off the surface normal direction. By changing the incident angle from the surface normal direction (z axis) to in-plane along the x-axis direction, the photonic bands in the $\Gamma - X$ direction can be obtained. The Γ point corresponds to the surface-normal incidence $\theta = 0°$. Here we mainly focus on a small value range of incident angle θ from 0° to 2°, which corresponds to the $k_\parallel$ range from 0 to ~0.01 ($2\pi/a$) in the vicinity of the bandedge. The spectral simulation is employed using the Fourier modal method with Stanford Stratified Structure Solver (S^4) software package [33]. In Fig. 1(b), the four bands in the normalized wavelength range (1520 nm, 1550 nm) are displayed with blue solid lines for the transverse electric (TE, or s) polarization, and red dashed lines for the transverse magnetic (TM, or p) polarization. One can see that all bands are very flat at the edges close to the Γ point, which indicates a very small group velocity and longer light-matter interaction time for these bandedge modes.

C. Analysis of Mode Properties

The field profiles of mode D at $\lambda = 1540$ nm are displayed in Fig. 1(c). The E-field of the standing-wave distribution is demonstrated with a red line, and the cavity index profile is plotted with a blue line. The confinement factor can be calculated as follows:

$$\Gamma_{QW} = \frac{\int_{QW} E^2 \bullet dv}{\int_{cav} E^2 \bullet dv}. \tag{1}$$

The quality factor and the field distribution of this cavity mode are also investigated. Their quality factor (Q) is obtained by Fano fitting the guided resonances in reflection spectra [34]. In our calculations, only the vertical radiation loss is considered as the in-plane loss, and the internal loss is negligible [23]. Hence, only the radiation loss is considered for the infinite cavity using the following relationship:

$$\alpha = \frac{2\pi}{Q \bullet a}. \tag{2}$$

Therefore, the gain threshold can be derived as follows:

$$g_{th} = \frac{\alpha}{\Gamma_{QW}}. \tag{3}$$

The E- field along the center of cavity (left) and the cross-section views of the E-field intensity of modes (right) are shown in Fig. 1(d). One can see the field is strongly confined inside the cavity due to a high index contrast above and below the laser cavity. Based on the above fundamental equations, the confinement factor, quality factor, and radiation loss of mode D
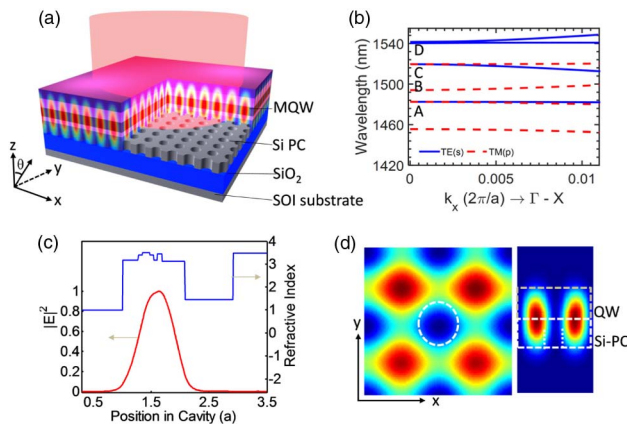

Fig. 1. (a) Schematic of PC bandedge membrane laser on SOI substrate; (b) photonic band diagram along $\Gamma - X$ direction of Si-PC bandedge membrane laser cavity structure, with the transferred InGaAsP QW mesas on top; (c) field distribution of cavity mode; (d) simulated field distributions.

Table 1. Calculated Values of the Quantities Γ_{QW}, Q, α, and g_{th}

Mode	Γ_{QW} (%)	Q	α (cm^{-1})	g_{th} (cm^{-1})
A	10.0	1.81e3	71.8	718.0
B	17.31	2.02e3	64.4	372.3
C	16.97	1.60e5	0.81	4.77
D	16.83	1.90e5	0.68	4.04

($\lambda = 1540$ nm) are calculated to be 16.83%, 1.9×10^5, and 0.68 cm^{-1}, respectively. The four different modes in the cavity close to the wavelength range of 1550 nm with various property schemes have been summarized in Table 1. The higher quality factor of the mode is due to a smaller hole radius and thicker thickness of Si-PC. The lasing oscillations are expected to be observed from all of these modes. Nevertheless, the dominated single-mode lasing spectrum predicted to occur at mode D corresponds to the lowest gain threshold of 4.04 cm^{-1}.

D. Coupling Efficiency

In particular, optical coupling phenomena in laser cavity are also investigated. The coupling coefficient for circular holes is expressed approximately as follows [30]:

$$\kappa \sim \frac{\pi \bullet \Gamma_{PC}}{a \bullet n_{eff^2}}(\varepsilon_{Si} - \varepsilon_{air}). \qquad (4)$$

The confinement factor of Si-PC (Γ_{PC}) is calculated to be around 37.7%. We discuss here the points that differ from our previous work. In our earlier design [15], the confinement factor of Si-PC (Γ_{PC}) was calculated to be around 4.56% and 46% for PCSEL-I and PCSEL-II, respectively. There is a 130 nm cladding layer underneath the InGaAsP MQW for PCSEL-I. For PCSEL-II, on the other hand, the InGaAsP MQW is directly built on the Si-PC without gap. We attribute the higher coupling efficiency mainly to the smaller separation distance between the InGaAsP MQW layer and Si-PC. Please note the confinement factor of Si-PC (Γ_{PC}) is proportioned to the separation distance in the cavity. In the present work (PCSEL-III), the separation distance is designed to be 70 nm, including a 30 nm cladding layer and a 40 nm contact layer for better current injection. One can see that more field distributed in the Si-PC region is indicative of a higher coupling efficiency of 37% for PCSEL-III. Also, the much-improved field confinement in the Si-PC region indicates a much stronger optical feedback in cavity. The calculated Q factor for the present design is 1.9×10^5, higher than previously reported cavity Q values [15]. Consequently, better lasing performances are achieved.

3. DEVICE FABRICATION

A SOI wafer with 230 nm top Si layer and 400 nm BOX layer was used here. The top Si layer was first thinned down to 190 nm by thermal oxidation and selective wet etching processes. Next, the 2D square lattice PC pattern with a size of 1 × 1 mm^2 was defined with ZEP-520 resist by using the standard electron beam lithography (EBL). The scanning electron microscopic (SEM) top view of Si-PC on SOI substrate is shown in Fig. 2(a). The lattice constant a and air hole radius r of the fabricated PC are 480 nm and 72 nm, respectively. The sample
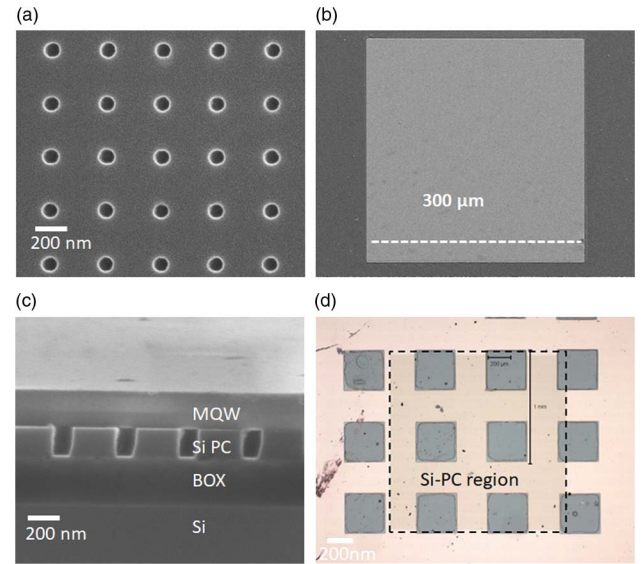

Fig. 2. (a) Zoomed-in SEM top view of the defect-free Si-PC cavity; (b) SEM image of InGaAsP MQW mesa transferred onto a Si-PC; (c) cross-sectional view of the cavity; (d) micrograph image of the transferred mesa array on a Si-PC.

was then etched with the ZEP-520 resist pattern to create a high index contrast between Si and air by using the dry etching process.

InGaAsP MQW structure was grown on (001) n-InP substrate by metal organic chemical vapor deposition (MOCVD), with a 500 nm InGaAs sacrificial layer between the top QW structure and the bottom InP substrate. Substrate removal and wax protection processes were used here for the release of the large area InGaAsP QW structure [15]. The transfer printing process was utilized to attach the InGaAsP MQW to the SOI substrate. The Si-PC on SOI substrate was first cleaned by solvent, followed by standard RCA cleaning to remove organic residues from the surface. The lifted InGaAsP MQW membrane is then carefully printed on a patterned Si-PC cavity. Subsequently, wax was removed with trichloroethylene (TCE) and isopropyl alcohol (IPA) solutions. Finally, a 300×300 μm^2 active MQW square size is defined by photolithography and selective wet etching process. Figures 2(b) and 2(c) show the SEM top view and cross-sectional view of a transferred InGaAsP MQW membrane on a Si-PC cavity on a SOI substrate. Shown in Fig. 2(d) is a micrograph image of PC bandedge membrane lasers on SOI substrate. It is worth noting that this process could be applied at room temperature and is capable of a 5 μm alignment accuracy.

4. DEVICE CHARACTERISTICS

Here we describe the lasing characteristics of the PC bandedge membrane laser. The device was optically pumped from the surface-normal direction via a long working distance objective lens (×10) by a continuous wave (cw) green (532 nm) laser. The diameter of the excitation spot is around 110 μm. The optical characteristics of this PC bandedge membrane laser device were then measured by a monochrometer based
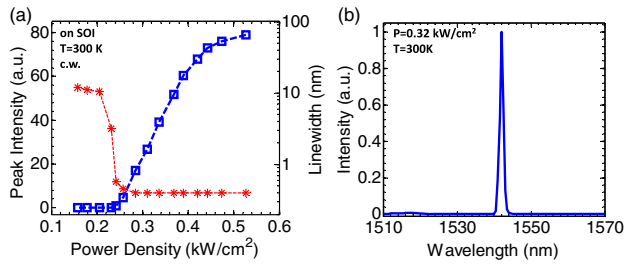
Fig. 3. (a) Lasing power and linewidth versus input power density at room temperature; (b) emission spectrum of the laser above threshold.

Fig. 5. (a) Schematic of PC bandedge membrane laser on bulk Si substrate; (b) cross-sectional view of the Si-PC bandedge membrane laser cavity structure on bulk Si substrate, with the transferred InGaAsP QW mesas on top; (c) field distribution of cavity mode; (d) simulated field distributions.

microphotoluminescence (μ-PL) setup. Figure 3(a) shows the light output and linewidth as a function of the pump power measured on the surface of the focusing plane. A threshold power density of 0.25 kW/cm² was obtained. The measured spectral linewidth was reduced from ∼14 nm (below threshold) to 0.54 nm (above threshold). Notice a thermal rollover was observed at optical pumping intensities higher than 0.4 kW/cm². A spectrum of the laser line above threshold is shown in Fig. 3(b), where the lasing wavelength is 1542 nm, very close to the predicted value of mode D in the simulation. The lower threshold pump power density is a result of the high Q value of mode D. All the other modes are possible to get lasing with sufficient pump energy.

Figure 4 shows the lasing spectrum measured at a pump power density of 0.32 kW/cm². A clear single-mode operation was observed. A zoomed-in lasing spectrum plotted in semilog scale is shown in Fig. 4(a). The peak wavelength, full width at half-maximum (FWHM) of the spectrum, and SMSR are 1542 nm, 0.54 nm, and 31.8 dB, respectively. Figure 4(b) is a measured far-field lasing profile with single-mode output at the focusing plane of the collimator.

5. LASER ON BULK SI SUBSTRATE

As mentioned above, the low-index BOX layer underneath the Si-PC layer limits the heat dissipation performance of the laser cavity due to relatively low thermal conductivity of oxide. Thus, it is of great importance to introduce the PC bandedge membrane laser directly built on bulk Si substrate, where the Si-PC structure is used as the bottom cladding layer, and the MQW membrane can be printed directly on bulk Si substrate
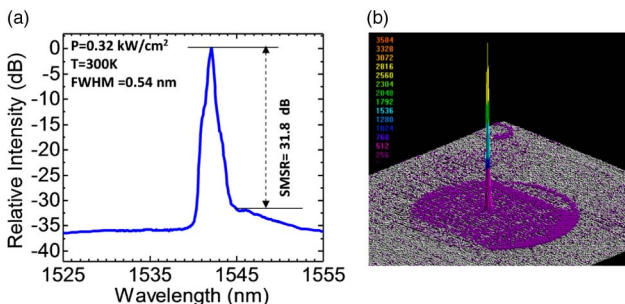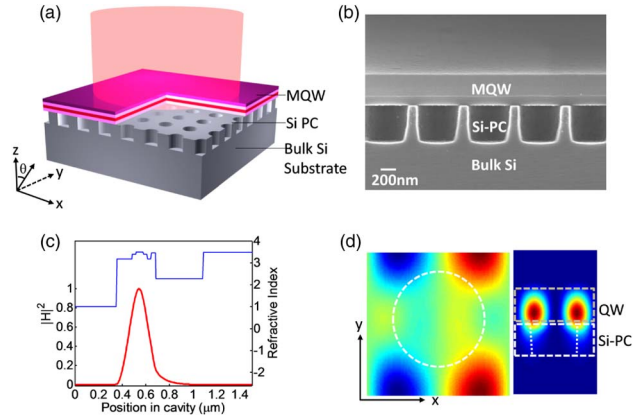
without a low-index oxide buffer layer. The design parameters were carefully chosen for the bottom Si-PC as smaller refractive index was involved as compared with laser on SOI substrate with low-index buffer. A schematic of a successful design of this structure is shown in Fig. 5(a), which consists of a transferred InGaAsP MQW membrane on a Si-PC cavity on a bulk Si substrate. A bulk Si wafer with 550 μm thickness was used here. The 2D square lattice PC pattern on bulk Si substrate was made following the same EBL patterning and dry etching processes. The SEM top view of Si-PC cavity on bulk Si substrate is shown in Fig. 5(b). The lattice constant (a), air hole radius (r), and etched depth of the fabricated PC are 540 nm, 243 nm, and 400 nm, respectively. The approximate refractive index n_{eff} of the InGaAsP MQW active layer and Si-PC was around 3.2 and 2.2 based on the average dielectric constant in the design. Different from the PC bandedge membrane laser on SOI substrate, the PC structure here was considered as the low refractive index cladding layer of the cavity. The field profile of the lasing mode is displayed in Fig. 5(c), where the integrated H-field intensity of the whole cavity along the z-axis direction is plotted together with the cavity index profile. The cross-section view of H-field intensity of lasing mode is shown in Fig. 5(d). Note here that the large air hole radius was designed to ensure the high refractive index contrast. One can see the field was confined inside the thin cavity due to high index contrast above and below the laser cavity. Moreover, the thickness of the Si-PC slab was chosen to be 400 nm to obtain high Q value by reducing the vertical radiation loss. Finally, the Q value of the lasing mode can be theoretically calculated around 3000, which would be able to achieve the single-mode lasing in the 160 K operation temperature [12].

To evaluate the laser performance experimentally, the PC bandedge membrane laser on bulk Si substrate was mounted on a temperature controlled stage inside a cryostat and characterized by the same microphotoluminescence (μ-PL) setup system in our previous work [11,12]. The measurement setup outlined is shown in Fig. 6. Figure 7(a) shows the light output and linewidth as a function of the pump power measured
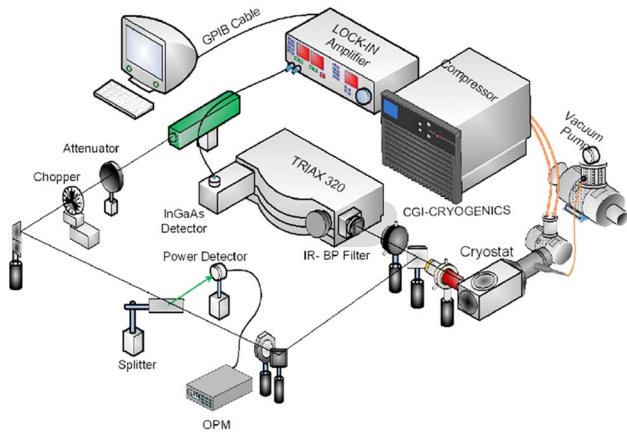

Fig. 4. (a) Lasing spectral output plotted in semilog scale above the pumping threshold; (b) 3D far-field laser profile.

Fig. 6. Schematic of the microphotoluminescence (μ-PL) setup system.
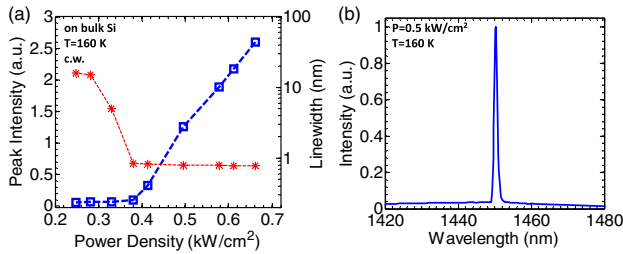

Fig. 7. (a) Lasing power and linewidth versus input power density at $T = 160$ K for PCSEL on bulk Si substrate; (b) emission spectrum of the laser above threshold.

on the surface of the PC bandedge membrane laser on bulk Si substrate. The laser threshold pump power density of 0.4 kW/cm^2 was obtained, where it was around a factor of 2 greater than PC bandedge membrane laser on SOI substrate at similar operation temperatures. We attribute this to the much lower optical confinement factor and less Q value within the cavity due to a larger air hole radius. The calculated Q factor is 3.27×10^3, which is 2 orders lower than the Q for PCSEL on SOI. However, there are few strategies to improve the laser characteristics of present cavity design on bulk Si substrate, such as the introduction of vertical asymmetry in the air-hole structure and effective utilization of tailoring the vertical etched profile. The Q value can be theoretically increased much higher above 3000, which would achieve lower threshold pump power density in the 160 K operation temperature. Figure 7(b) presents the measured lasing spectrum above the threshold. The single-mode lasing peak wavelength and linewidth are 1452 nm and 0.87 nm in the 160 K operation temperature.

6. THERMAL PERFORMANCE ANALYSIS

In order to compare the thermal performance, here we prepared two PC bandedge membrane lasers built onto bulk Si substrate and SOI substrate, respectively. The laser cavity for both devices is designed to operate at similar temperatures and emission wavelengths. The thicknesses of each layer of the InGaAsP

Table 2. Cavity Design Structure of Laser on Bulk Si and SOI

Layer Materials	Laser on Bulk Si	Laser on SOI
p-InP	130 µm	
InGaAsP	127 µm	
MQW		
n-InP	130 µm	
n-InGaAs	40 µm	
Si-PC	400 nm, $a = 540$ nm $r/a = 0.45$	190 nm, $a = 480$ nm $r/a = 0.15$
SiO$_2$	0	400 nm
Si substrate	525 µm	

MQW membrane and the parameter of Si-PC are listed in Table 2.

The bulk Si substrate is expected to dissipate more heat along the vertical direction from the surface of the cavity to the bottom substrate and heat sink. A figure of merit to quantify the heat dissipation out of the cavity is the thermal resistance [35,36]. By extracting the shift of emission peak wavelength with varying the temperature and pump power, the thermal resistance of the laser can be mathematically defined by the following ratio:

$$R_{\text{th}} = \frac{\left.\frac{\Delta\lambda}{\Delta P_{\text{heat}}}\right|T = \text{const.}}{\left.\frac{\Delta\lambda}{\Delta T}\right|P = \text{const.}} \sim \frac{\left.\frac{\Delta\lambda}{\Delta P_p}\right|T = \text{const.}}{\left.\frac{\Delta\lambda}{\Delta T}\right|P = \text{const.}}. \quad (5)$$

Here, the ΔP_{heat} is the heat generated from the cavity, and ΔP_p is the total pump power. We assume heat generation is primarily in the QW section [37], and it is linearly proportional to the optical pump power for the operation window between threshold and rollover. We first characterize the PC bandedge membrane laser on bulk Si substrate. The wavelength spectrum dependence of the pumping power from the PC bandedge membrane laser on bulk Si substrate was measured, as shown in Fig. 8(a). The peak of the emission wavelength slightly shifted towards longer wavelengths when the pump power increased from 25 mW to 50 mW at 160 K. In our measurement, the spectral shift versus power ratio presents the spectral shift versus power generated from the QW region. Second, the spectral dependence of the operation temperature varying from 120 to 200 K at a constant incident power was also measured and
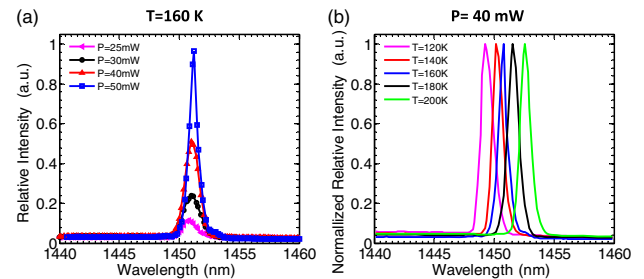

Fig. 8. (a) Lasing spectra at different pump powers above threshold at constant 160 K; (b) lasing spectra at different operation temperatures with constant 40 mW pump power.
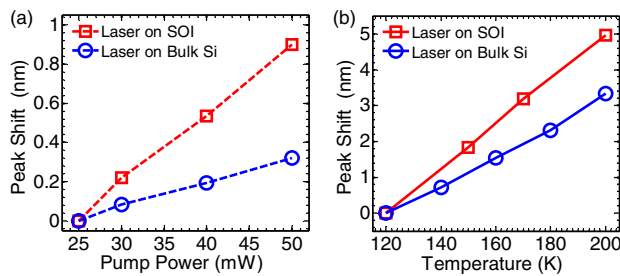
Fig. 9. (a) Emission peak wavelength shift versus pump powers for PC bandedge membrane laser on SOI and on bulk Si substrate; (b) emission peak wavelength shift versus operation temperatures for PC bandedge membrane laser on SOI and on bulk Si substrate.

shown in Fig. 8(b). Please note the cavity design of the PC bandedge membrane laser on bulk Si substrate was optimized for device operation around 160 K. Single-mode lasing operation was obtained at the 120 to 200 K range for the pump power at 40 mW. The wavelength shift versus pumping power was calculated to be 0.0125 nm/mW, and the shift versus temperature was 0.0412 nm/K.

Figures 9(a) and 9(b) show the measured emission wavelength peak shift at different pump powers and varying operation temperatures for both PC bandedge membrane lasers on bulk Si substrate and on SOI substrate operation at 160–180 K. For the PC bandedge membrane laser on bulk Si substrate, the thermal resistance was extracted from Figs. 9(a) and 9(b) and calculated to be 303.4 K/W. On the other hand, the thermal resistance of the PC bandedge membrane laser on SOI was calculated to be 558.5 K/W. The thermal resistance of the PC bandedge membrane laser on bulk Si substrate is therefore around a factor of 2 times lower than that of a structure with a BOX layer. We attributed the higher thermal resistance to the low thermal conductivity of the BOX layer. It is also worth noting that the thermal resistance value calculated here is a relative value, as the absolute value should be based on the exact heat source (ΔP_{heat}), which is not known here.

7. CONCLUSIONS

We successfully demonstrated a hybrid III-V/Si-PC bandedge membrane laser, based on a transferred InGaAsP MQW structure on Si substrate. With the careful cavity design, single-mode lasing under room temperature optical pumping was achieved with a linewidth ~5.4 Å and a SMSR of 31.8 dB. Another important cavity design of the PC bandedge membrane laser directly built on bulk Si substrate was also reported. The excellent heat dissipation from the active region and minimized temperature rise of the lasing cavity were also demonstrated experimentally, and agree well with the simulation.

REFERENCES

1. G. Roelkens, L. Liu, D. Liang, R. Jones, A. Fang, B. Koch, and J. Bowers, "III-V/silicon photonics for on-chip and intra-chip optical interconnects," Laser Photon. Rev. **4**, 751–779 (2010).
2. D. M. Gill, C. Xiong, J. E. Proesel, J. C. Rosenberg, J. Orcutt, M. Khater, J. Ellis-Monaghan, D. Viens, Y. Vlasov, W. Haensch, and W. M. J. Green, "Demonstration of error free operation up to 32 Gb-s from a CMOS integrated monolithic nano-photonic transmitter," in *Conference on Lasers and Electro-Optics (CLEO)* (2015), paper STu4F-3.
3. K. Xu, "Electro-optical modulation processes in Si-PMOSFET LEDs operating in the avalanche light emission mode," IEEE Trans. Electron. Devices **61**, 2085–2092 (2014).
4. D. A. B. Miller, "Device requirements for optical interconnects to silicon chips," Proc. IEEE **97**, 1166–1185 (2009).
5. R. Soref, "The achievements and challenges of silicon photonics," Adv. Opt. Technol. **2008**, 1–7 (2008).
6. R. Soref, "The past, present, and future of silicon photonics," IEEE J. Sel. Top. Quantum Electron. **12**, 1678–1687 (2006).
7. L. Pavesi, "Will silicon be the photonic material of the third millenium?" J. Phys. Condens. Matter **15**, R1169–R1196 (2003).
8. K. Xu, L. W. Snyman, and H. Aharoni, "Si light-emitting device in integrated photonic CMOS ICs," Opt. Mater. **69**, 274–282 (2017).
9. H. Park, A. W. Fang, O. Cohen, R. Jones, M. J. Paniccia, and J. Bowers, "Design and fabrication of optically pumped hybrid silicon-AlGaInAs evanescent lasers," IEEE J. Sel. Top. Quantum Electron. **12**, 1657–1663 (2006).
10. J. Van Campenhout, P. Rojo-Romeo, P. Regreny, C. Seassal, D. Van Thourhout, S. Verstuyft, L. Di Cioccio, J.-M. Fedeli, C. Lagahe, and R. Baets, "Electrically pumped InP-based microdisk lasers integrated with a nanophotonic silicon-on-insulator waveguide circuit," Opt. Express **15**, 6744–6749 (2007).
11. R. Chen, T.-T. D. Tran, K. W. Ng, W. S. Ko, L. C. Chuang, F. G. Sedgwick, and C. J. Chang-Hasnain, "Nanolasers grown on silicon," Nat. Photonics **5**, 170–175 (2011).
12. Z. Mi, P. Bhattacharya, J. Yang, and K. P. Pipe, "Room-temperature self-organised $In_{0.5}Ga_{0.5}As$ quantum dot laser on silicon," Electron. Lett. **41**, 742–744 (2005).
13. S. Chen, W. Li, J. Wu, Q. Jiang, M. Tang, S. Shutts, S. N. Elliott, A. Sobiesierski, A. J. Seeds, I. Ross, P. M. Smowton, and H. Liu, "Electrically pumped continuous-wave III-V quantum dot lasers on silicon," Nat. Photonics **10**, 307–311 (2016).
14. H. Yang, D. Zhao, S. Chuwongin, J.-H. Seo, W. Yang, Y. Shuai, J. Berggren, M. Hammar, Z. Ma, and W. Zhou, "Transfer-printed stacked nanomembrane lasers on silicon," Nat. Photonics **6**, 617–622 (2012).
15. D. Zhao, S.-C. Liu, H. Yang, Z. Ma, C. Reuterskiöld-Hedlund, M. Harrmar, and W. Zhou, "Printed large-area single-mode photonic crystal bandedge surface-emitting lasers on silicon," Sci. Rep. **6**, 18860 (2016).
16. P. Chaisakul, D. Marris-Morini, J. Frigerio, D. Chrastina, M.-S. Rouifed, S. Cecchi, P. Crozat, G. Isella, and L. Vivien, "Integrated germanium optical interconnects on silicon substrates," Nat. Photonics **8**, 482–488 (2014).
17. K. Xu, K. A. Ogudo, J.-L. Polleux, C. Viana, Z. Ma, Z. Li, Q. Yu, G. Li, and L. W. Snyman, "Light emitting devices in Si CMOS and RF bipolar integrated circuits," J. Illum. Eng. Soc. **12**, 203–212 (2016).
18. N. Sherwood-Droz and M. Lipson, "Scalable 3D dense integration of photonics on bulk silicon," Opt. Express **19**, 17758–17765 (2011).
19. G. Kim, H. Park, J. Joo, K.-S. Jang, M.-J. Kwack, S. Kim, I. G. Kim, J. H. Oh, S. A. Kim, J. Park, and S. Kim, "Single-chip photonic transceiver based on bulk-silicon, as a chip-level photonic I/O platform for optical interconnects," Sci. Rep. **5**, 11329 (2015).

20. B. Song, C. Stagarescu, S. Ristic, A. Behfar, and J. Klamkin, "3D integrated hybrid silicon laser," Opt. Express **24**, 10435–10444 (2016).

21. K. Xu, "Integrated silicon directly modulated light source using p-well in standard CMOS technology," IEEE Sens. J. **16**, 6184–6191 (2016).

22. M. Imada, A. Chutinan, S. Noda, and M. Mochizuki, "Multi-directionally distributed feedback photonic crystal lasers," Phys. Rev. B **65**, 195306 (2002).

23. K. Hirose, Y. Liang, Y. Kurosaka, A. Watanabe, T. Sugiyama, and S. Noda, "Watt-class high-power, high-beam-quality photonic-crystal lasers," Nat. Photonics **8**, 406–411 (2014).

24. M. Imada, S. Noda, A. Chutinan, T. Tokuda, M. Murata, and G. Sasaki, "Coherent two-dimensional lasing action in surface-emitting laser with triangular-lattice photonic crystal structure," Appl. Phys. Lett. **75**, 316–318 (1999).

25. S.-L. Chua, L. Lu, J. Bravo-Abad, J. D. Joannopoulos, and M. Soljačić, "Larger-area single-mode photonic crystal surface-emitting lasers enabled by an accidental Dirac point," Opt. Lett. **39**, 2072–2075 (2014).

26. M. Meier, A. Mekis, A. Dodabalapur, A. Timko, R. E. Slusher, J. D. Joannopoulos, and O. Nalamasu, "Laser action from two-dimensional distributed feedback in photonic crystals," Appl. Phys. Lett. **74**, 7–9 (1999).

27. S. Noda, M. Yokoyama, M. Imada, A. Chutinan, and M. Mochizuki, "Polarization mode control of two-dimensional photonic crystal laser by unit cell structure design," Science **293**, 1123–1125 (2011).

28. L. J. Martínez, B. Alan, I. Prieto, J. F. Galisteo-Lopez, M. Galli, L. C. Andreani, C. Seassal, P. Viktorovitch, and P. A. Postigo, "Two-dimensional surface emitting photonic crystal laser with hybrid triangular-graphite structure," Opt. Express **17**, 15043–15051 (2009).

29. Y. Sato, Y. Tanaka, J. Upham, Y. Takahashi, T. Asano, and S. Noda, "Strong coupling between distant photonic nanocavities and its dynamic control," Nat. Photonics **6**, 56–61 (2012).

30. K. Sakai, E. Miyai, and S. Noda, "Coupled-wave model for square-lattice two-dimensional photonic crystal with transverse-electric-like mode," Appl. Phys. Lett. **89**, 021101 (2006).

31. Y. Kurpsaka, S. Iwahashi, K. Sakai, E. Miyai, W. Kunishi, D. Ohnishi, and S. Noda, "Band structure observation of 2D photonic crystal with various V-shaped air-hole arrangements," IEICE Electron. Express **6**, 966–971 (2009).

32. J. Lee, B. Zhen, S.-L. Chua, W. Qiu, J. D. Joannopoulos, M. Soljacic, and O. Shapira, "Observation and differentiation of unique high-Q optical resonances near zero wave vector in macroscopic photonic crystal slabs," Phys. Rev. Lett. **109**, 067401 (2012).

33. V. Liu and S. Fan, "S⁴: a free electromagnetic solver for layered periodic structures," Comput. Phys. Commun. **183**, 2233–2244 (2012).

34. B. Luk'yanchuk, N. I. Zheludev, S. A. Maier, N. J. Halas, P. Nordlander, H. Giessen, and C. T. Chong, "The Fano resonance in plasmonic nanostructures and metamaterials," Nat. Mater. **9**, 707–715 (2010).

35. T. Flick, K. H. Becks, J. Dopke, P. Mattig, and P. Tepel, "Measurement of the thermal resistance of VCSEL devices," J. Instrum. **6**, C01021 (2011).

36. J. Ferrara, W. Yang, L. Zhu, P. Qiao, and C. J. Chang-Hasnain, "Heterogeneously integrated long-wavelength VCSEL using silicon high contrast grating on an SOI substrate," Opt. Express **23**, 2512–2523 (2015).

37. H. Lindberg, M. Strassner, E. Gerster, J. Bengtsson, and A. Larsson, "Thermal management of optically pumped long-wavelength InP-based semiconductor disk lasers," IEEE J. Sel. Top. Quantum Electron. **11**, 1126–1134 (2005).